 https://doi.org/10.3311/PPme.37086

Periodica Polytechnica Mechanical Engineering, 68(3), pp. 216–224, 2024

Can the Flow Simulation Domain for Bifurcation Aneurysms on the Willis Circle Be Radically Reduced?

Péter Friedrich[1], György Paál[1]

[1] Department of Hydrodynamic Systems, Faculty of Mechanical Engineering, Budapest University of Technology and Economics, Műegyetem rkp. 3., H-1111 Budapest, Hungary
* Corresponding author, e-mail: pfriedrich@hds.bme.hu

Received: 09 April 2024, Accepted: 26 July 2024, Published online: 02 August 2024

Abstract

This paper presents an attempt to decrease the domain for the simulation of blood flow in certain types of bifurcation aneurysms. A reduced computational cost would be beneficial for the simulation of large datasets, to have statistical data for various hemodynamical parameters. The reduction is achieved by cutting the geometry in an objective manner, with the help of the Vascular Modelling Toolkit (VMTK). CFD simulations were carried out on both the original and the partial geometries, using partially patient-specific boundary conditions. The post-processing focused on the velocity field, as it is more robust than the wall shear stress-based indicators for aneurysm formation. Using VMTK, a centerline was calculated for each case. Various morphological values can be calculated, namely the torsion and curvature. The velocity field was broken down to velocity components using the Frenet-frames. The evaluation was carried out on a plane before the next bifurcation downstream. The post-processing calculations were made for 2 distinct time steps, one at the systolic and one at the diastolic instant and for a cycle average. The results showed that the method reproduces the axial velocity component with small deviations. However, for the secondary components the difference between the partial and original geometries was unacceptably high. Therefore, the method proved to be unsuitable.

Keywords

secondary flows, bifurcation aneurysm, hemodynamics

1 Introduction

Cardiovascular diseases are still leading causes of death and lifelong disabilities. Cerebral aneurysms are sac-like malformations, manifesting on the side of an artery or more prominently at bifurcation sites. Bifurcation aneurysms form at junctions of the blood vessels, on the opposite side of the parent vessel. In case of rupture brain hemorrhage can occur leading to devastating consequences. Both morbidity and mortality are high. However, the risk of a rupture is relatively low [1–3]. Unfortunately, cerebral aneurysms do not have typical symptoms, so they are usually discovered accidentally during unrelated medical imaging of brain arteries.

Understanding the underlying biomechanical effects and processes of aneurysm initiation could be beneficial to help predict and treat aneurysms better. It is accepted that a complex biomechanical response of the vessel wall to changing flow conditions causes the formation of the aneurysm. Pressure and wall shear stress (WSS) are the mechanical stimuli which can be felt by the innermost layer of the wall, the internal elastic lamina [4]. Thus, the first studies into the initiation of aneurysms focused on these metrics. There are two main theories for the formation of aneurysms, the low-flow and the high-flow theories. The low-flow theory argues that the slower velocity in the aneurysm causes the stagnation of the blood, which is suspected to induce the inflammatory processes. The high-flow theory suggests that high value of WSS can cause damage in the vessel wall and induce the formation process [5–9].

In recent years as technology progressed, medical imaging has become increasingly widespread. Hence, the number of discovered aneurysms increased significantly. From medical images, it is possible to create a 3D computer model of the blood vessels. A public aneurysm database was created, called Aneurisk [10], where aneurysms are categorized and often have the 3D models available as well. The availability of models opened the research on aneurysm formation, using computational methods. A key

Cite this article as: Friedrich, P., Paál, G. "Can the Flow Simulation Domain for Bifurcation Aneurysms on the Willis Circle Be Radically Reduced?", Periodica Polytechnica Mechanical Engineering, 68(3), pp. 216–224, 2024. https://doi.org/10.3311/PPme.37086

part of the computational approach is the digital reconstruction of the vessel to a pre-aneurysm state. The growing number of discovered aneurysms mean that there are now medical images available after the formation of the sac. This necessitates the removal of the sac, and the restoration of the blood vessels to a pre-disease state to be able to understand the cause of aneurysm formation. Objective mathematical methods have been developed for this task, both for side wall [11] and bifurcation aneurysms [12].

The other key computational tool is Computational Fluid Dynamics (CFD). Using CFD it is possible to simulate the blood flow inside the vessel, and compute various biomechanical indicators measured at the wall [13]. As wall-based methods highly depend on the exact surface geometry of the wall, they carry uncertainties, due to the subjective elements of the segmentation process [14, 15]. On the other hand, the velocity field is more robust, and is less sensitive to small surface features of the wall. Our hypothesis is that secondary flow plays a significant role in the initiation of the aneurysm [16].

Important components of numerical simulations are the boundary conditions. Selecting the wrong boundary conditions can produce wrong results. When applicable, the boundary conditions are based on measurement data. For a long time only generalized boundary conditions were used in this field. In recent years various partially patient-specific methods emerged, based on Murray's law [17, 18]. These approximate the flow rate, based on the cross-sectional area of the vessel. One such method is implemented in Aneutools [19], an open-source Python toolkit. It can be used to compute boundary conditions for the internal carotid artery. However, bifurcation aneurysms often form in the deeper parts of the brain, downstream from the internal carotid artery (ICA). In a previous work [20] the boundary conditions were calculated using Aneutools from the ICA inlet. This resulted in simulation domains starting from the ICA inlet and going into the Willis circle. The numerical meshes for the simulations were thus large, which resulted in a very high computational cost.

The goal of this paper is to explore a method to radically cut down on the size of the computational domain to decrease the computational cost, while keeping the accuracy of the simulations, focusing on the secondary flow field.

By shrinking the simulation domain, the time and resources required for a case decrease, thus helping the simulation of large datasets.

2 Methodology

2.1 Geometry generation

Seven geometries were studied in this research. Five were chosen from the Aneurisk database (IDs starting with C). The other two were obtained through the National Brain Research program of Hungary (IDs starting with NAP). The study was conducted according to the guidelines of the Declaration of Helsinki and approved by the Institutional Review Board (or Ethics Committee). None of them had bifurcation aneurysms in the examined section. A difference for bifurcation aneurysm compared to side wall aneurysms is that control cases are absolutely required for evaluating the flow at the aneurysm site. For this reason, geometries and sections were chosen, where the examined bifurcation did not have an aneurysm.

The geometries from the Aneursik database were available as 3D models. Those from the National Brain Research Program were available as DICOM images. These were segmented using 3D Slicer [21] to 3D geometries. The surface of the segmented geometries was smoothed using the Taubin smoothing [22] algorithm.

The geometries were cut in an objective manner, using the Vascular Modelling Toolkit (VMTK) [23, 24]. The first step of the procedure was to calculate the centerline of the geometry in question. The centerline starts from the inlet and reaches all the outlets of the geometry. As the centerline branches at bifurcations, bifurcation regions could be marked objectively using VMTK. Using these regions, cutting planes were defined at given distances from the bifurcation perpendicularly to the centerline.

Apart from the last step, the procedure described above was carried out automatically by the VMTK package. The distance of the cutting planes was roughly 3 diameters after the bifurcation, at the nearest point on the centerline. The cutting plane can be seen in Fig. 1 in green. The cut was made in Paraview [25]. The resulting model was then exported as an open surface mesh for the remaining pre-processing. Open surface means that the inlet and outlets were not closed by surfaces.

Both the original and the partial model were modified further to prepare them for computational fluid dynamics simulations. The inlet and the outlets were extended by straight pipe sections of 8 diameter to dampen the numerical effects of the boundaries. In the last step, the open boundaries were closed and a final remeshing is carried out to ensure proper surface triangle quality. This was required because the straight extensions and the rest of the

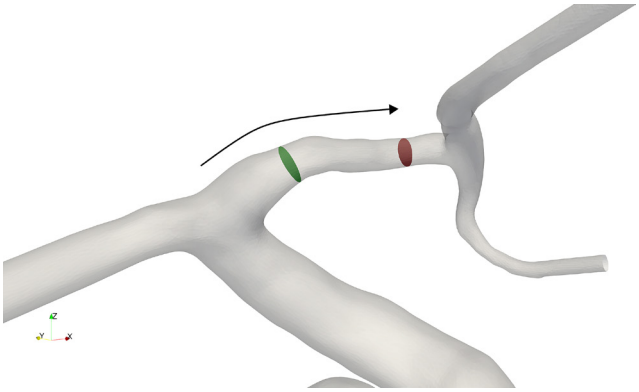

Fig. 1 The cutting plane in green, and the plane used for the post-processing in red, the arrow indicates the direction of the flow

geometry can have differently sized triangles. The final original and partial geometries are shown in Fig. 2. NAP200909C is shown in Fig. 3 in more detail.

A section of an artery can be described by multiple morphological properties, which capture the geometry of the artery section.

Tortuosity describes, how curved the artery is. It is the ratio of the length of the artery on the centerline (C) and the distance between the endpoints in a straight line (L). A number close to 1 means the section in question is almost straight, while a high number means that the artery is highly tortuous.

$$\text{Tortuosity} = \frac{C}{L} \tag{1}$$

By using Frenet-frames [26], the curvature (κ) and torsion (τ) of the centerline can be calculated, using VMTK. Curvature is the inverse of the radius of the osculating circle at a given point. Torsion describes the rotation of the

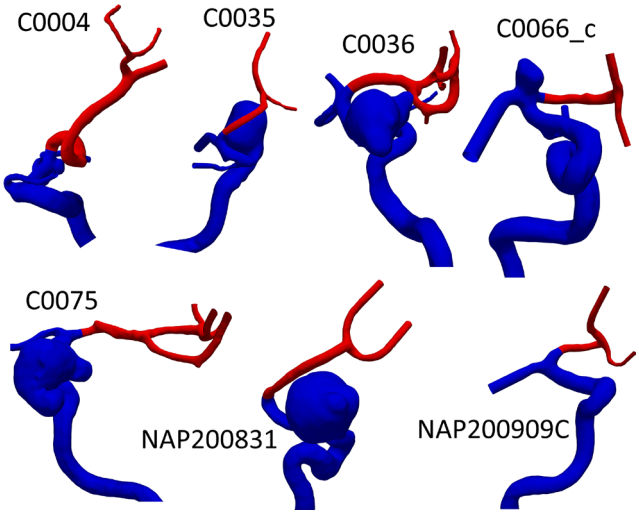

Fig. 2 The geometries, original in blue and red, and the partial in red

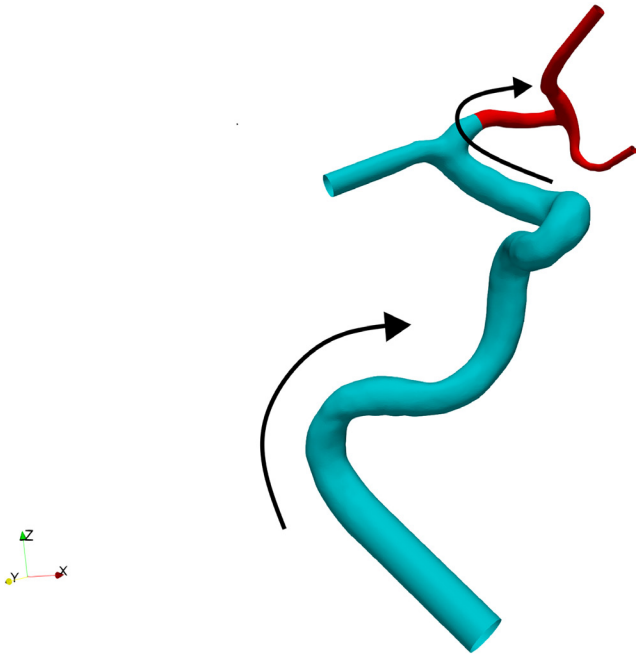

Fig. 3 The original geometry (blue and red) and the partial geometry (red), the arrows indicate the direction of the flow

binormal vector in the Frenet-frame [23]. These quantities were averaged over the region of interest, between the cutting plane and a plane 3 diameter lengths before the next bifurcation. The maximum inscribed sphere radii were also averaged to be used as a diameter-like parameter. Using the latter and the length of the centerline between the two planes, a relative length, L/D, was also calculated. Table 1 shows these morphological parameters.

2.2 Simulations

Seven different patient-specific cases were studied, so that altogether 14 simulations were performed. The cases were chosen from the Aneurisk database and from our medical partners. The examined sections started from the internal carotid artery and continued through the carotid terminating bifurcation till the outlets of the next bifurcation downstream.

The meshing and the simulations were carried out using the ANSYS 22 R2 software package [27]. The mesh was

Table 1 Morphological features of the geometries

ID	Tortuosity	L/D	Curvature	Torsion
C0004	1.69939	26.87775	0.23802	0.00340
C0035	1.09313	16.97156	0.12162	0.13741
C0036	1.05120	8.59790	0.08435	-0.00915
C0066	1.03343	14.20108	0.08440	0.54805
C0075	1.07974	11.58881	0.14491	0.36201
NAP200831	1.07363	20.57279	0.09332	0.07871
NAP200909C	1.03643	8.74769	0.09300	0.47756

made of tetrahedral cells with an edge size of 0.1 mm. An inflation layer was applied at the walls, with a growth rate of 1.1 and 10 layers, resulting in a first layer thickness of 0.015 mm. The target value for the skewness was set to 0.8. The same settings were used for both the original geometry and the partial one. On average the partial geometry had about 80% fewer cells than the original geometry.

Blood was modelled as a Newtonian fluid [28–30]. The density was 1055 kg/m^3 and the dynamic viscosity 0.0034 Pas. No turbulence model was used, as the Reynolds number was below 1000 in all cases. The wall of the geometry was assumed to be rigid, which is an accepted simplification in the literature [31].

2.3 Original geometry boundary conditions

For CFD simulations the selection of the correct boundary conditions is crucial. In the case of hemodynamics, it is hard to define a patient-specific boundary condition, especially for arteries in the brain. General boundary conditions are often used, but various semi patient-specific boundaries do exist. One such option is [17] which can be used to calculate a mass flow rate average for the ICA inlet based on its cross-sectional area using Murray's law. From the calculated mass flow rate average, a mean velocity is calculated. This average is for one heart cycle in the inlet cross-section. So, by using a heart cycle signal [32], the velocity average in the cross-section can be calculated for every time step in the cycle. A parabolic velocity inlet profile was set as an inlet with the cross-sectional average of the profile. The cross-sectional average velocity was computed for each time step.

The outlets were set as mass flow outlets, except for the smallest one, which was set to opening with a constant relative pressure of 0 Pa. The mass flow for each outlet was calculated with Aneutools [18], which also uses the flow-area relationship to calculate a percentage of the outflow for each outlet. These were calculated for each time step, based on the mass flow rate of the inlet.

2.4 Partial geometry boundary conditions

For the partial geometries the boundary conditions were of the same type, but their calculations were slightly different.

First, the outlet flow rate percentages were summed up. The inlet mass flow rate of the original case was multiplied by this summed up percentage to get the average inlet mass flow rate for the partial geometry. Then an average velocity was calculated using the cross-sectional area of the inlet on the partial geometry. A velocity was calculated for every time step using the virtual heart cycle signal. A parabolic velocity profile was also prescribed in the cross-section.

The outlets were set as mass flow outlets, calculated using Aneutools. The smallest outlet was set as an opening with 0 Pa relative pressure. This was not necessarily the same outlet as in the original geometry.

2.5 Post processing

The post-processing focused on cross-sections 3 diameter lengths before the next bifurcation after the cutting plane. The plane of the post-processing is shown in Fig. 1 in red. The velocity profiles were examined on two orthogonal lines defined with the Frenet-system. One was in line with the normal vector and the other was in line with the binormal vector. The lines were defined by their end points, located at 1.1 times the maximum inscribed spheres diameter apart. The line was sampled by 1000 points placed uniformly along the line. Because of the surface remeshing step the walls of the original and partial geometry were slightly different. To solve this problem, the values of the partial geometries were resampled at the same points as in the original geometry. Points outside the vessel wall were removed during the post-processing.

The velocity differences between the partial and the original geometries were calculated by subtracting the values of the partial geometry from the values of the original one on a point-by-point basis.

Using the Frenet-frames, the velocity field can be decomposed into an axial and a secondary component [26].

Scripts calculated the axial and secondary velocity components for the systolic and diastolic instances, and for the cycle average. It also calculated the difference between the velocity profiles between the original and partial geometries.

3 Results and discussion

3.1 Flow rate

To check the feasibility of the method, the volumetric flow rate was calculated and compared between the original and the partial geometries. This was checked because the smallest outlet with a 0 Pa boundary condition was not always on the partial geometry. It is shown in Table 2. The flow rate in original and the partial section were measured on the post-processing plane. The differences are small, in all cases below 1%.

Table 2 Volume flowrate difference between the full and partial geometries

ID	Q original [m³/s]	Q partial [m³/s]	Difference
C0004	$2.17 \cdot 10^{-7}$	$2.19 \cdot 10^{-7}$	−0.982%
C0035	$4.73 \cdot 10^{-7}$	$4.73 \cdot 10^{-7}$	−0.073%
C0036	$7.79 \cdot 10^{-7}$	$7.80 \cdot 10^{-7}$	−0.160%
C0066	$1.87 \cdot 10^{-7}$	$1.89 \cdot 10^{-7}$	−0.893%
C0075	$3.40 \cdot 10^{-7}$	$3.41 \cdot 10^{-7}$	−0.200%
NAP200831	$4.82 \cdot 10^{-7}$	$4.80 \cdot 10^{-7}$	0.474%
NAP200909C	$8.42 \cdot 10^{-7}$	$8.44 \cdot 10^{-7}$	−0.293%

3.2 Velocity field

The results from the velocity field are shown as profiles first. Then the difference between the profiles is shown as box plots, to better show the distribution of the differences between the original and partial geometries.

3.2.1 Velocity profiles

Velocity profiles were plotted for each geometry from the cycle averaged results on the Frenet normal line. These can be seen in Fig. 4. The axial velocity is shown in red, and the secondary magnitude in blue. The solid lines represent the original geometry, and the dashed ones represent the partial ones.

Except for C0066_c the axial velocity profiles show good agreement. The profiles of C0066_c have similar shapes but differ in maximum values. The partial geometry has a 24% lower maximum for the profile.

The secondary velocity profiles show much worse results. For most cases the profiles for the original and partial geometry still show similar shapes, but the agreement between the two profiles is worse than in the case of the quantitative axial velocity profiles. Among the secondary velocity profiles NAP200909C has the worst results. The shape of the profile for the partial geometry does not look similar to the profile of the original geometry. The maximum value of the profile is also lower by 16%. C0066_c and C0075 have similarly shaped profiles. In the case of C0066_c the secondary velocity is lower in the partial geometry than the original geometry by 42%. In contrast, for C0075 it is 27% higher in the partial geometry than in the original geometry. The angle of the secondary velocity vectors showed similar tendency to the magnitudes of the secondary velocity profiles.

3.2.2 Axial velocity difference

First, the axial velocity difference is presented. In the systolic instance of the heart cycle the median of the difference is mostly below 5%, except for the outlier, C0066_c, as seen in Fig. 5. For C0066_c median is 22% The difference increases as the average torsion increases. In the time-averaged results, the differences decrease, and the highest median is below 5%, while most are below 3% as seen in Fig. 6. These differences are higher than the difference in volumetric flowrate, although the axial velocity

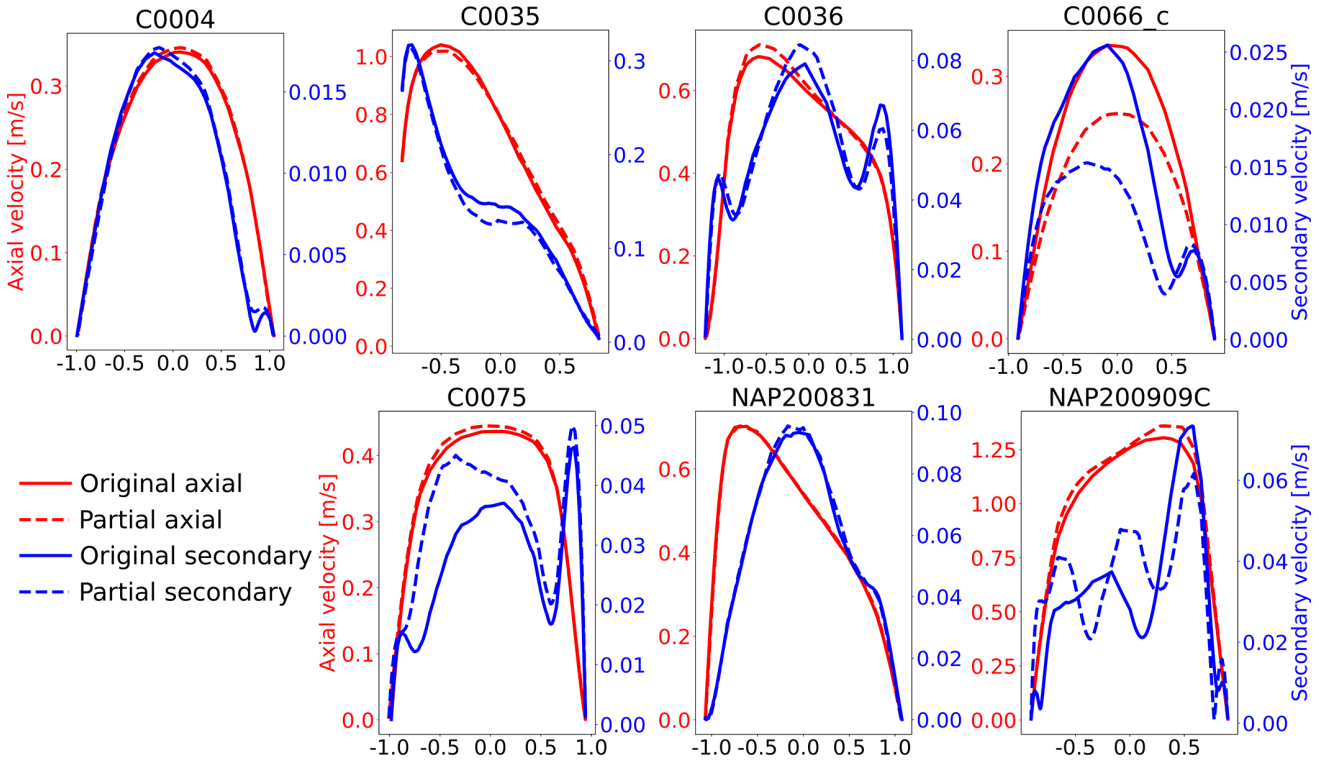

Fig. 4 Velocity profiles for each geometry in the systolic time instance in red, secondary velocity magnitude profiles in blue

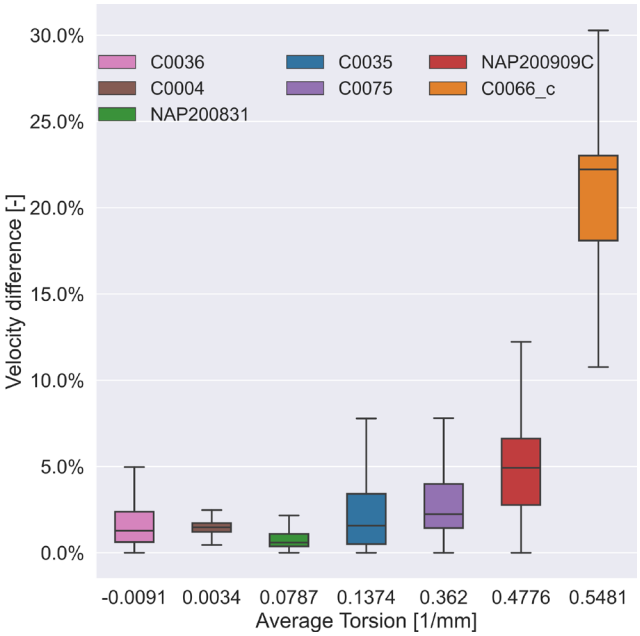

Fig. 5 Velocity difference graph for the axial component, in systolic time instant in relation to the average torsion

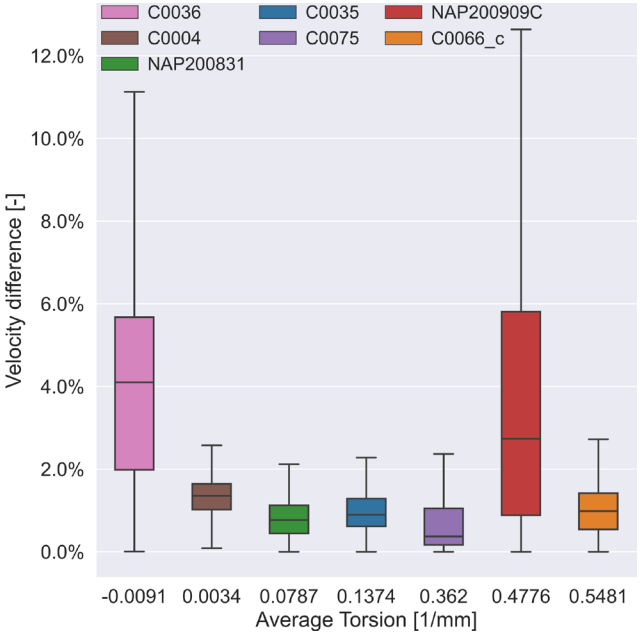

Fig. 6 Velocity difference graph for the axial component, cycle averaged

expresses the bulk flow. The difference is caused by the different methods. The volume flowrate was calculated by integrating the velocity field over the cross-section, while the velocity components were only calculated on two lines of the cross-section.

3.2.3 Secondary velocity field

The secondary velocity field in the diastolic time instant is shown in Fig. 7, most IQRs are between 2% and 17%, with the medians being below 10%. There are two outliers,

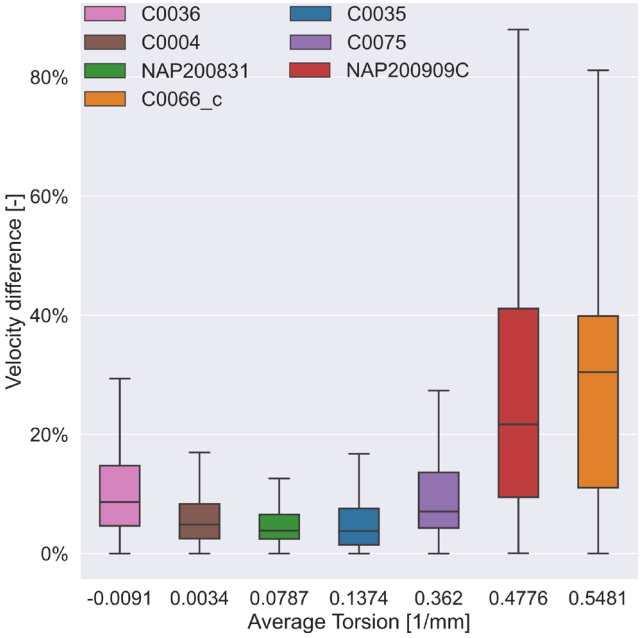

Fig. 7 Velocity difference graph for the secondary component, in diastolic time instant in relation to the average torsion

these are C0066 and NAP200909C. These not only have higher medians with 22% and 31% respectively, but their respective IQRs span a wider range, reaching as high as 41%. These are the same cases, where the velocity profiles showed the largest differences.

For the systolic time instant the differences increase for some cases and are shown in Fig. 8. The third quartile can reach as high as 81% and the maxima over 150%. Though

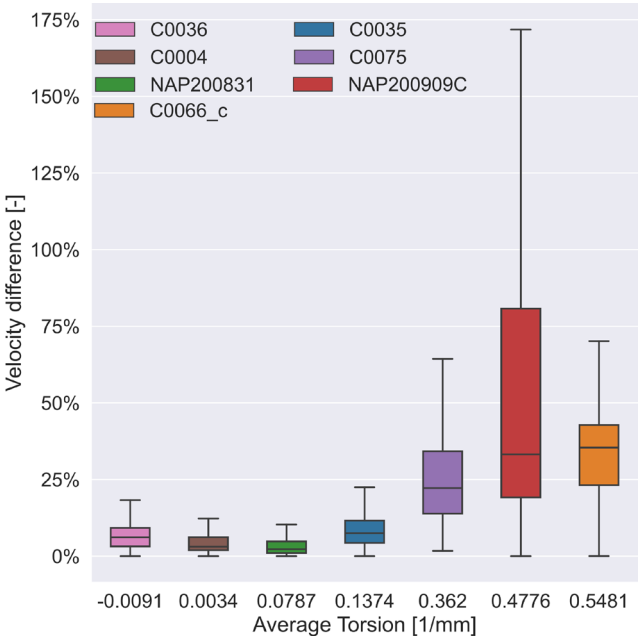

Fig. 8 Velocity difference graph for the secondary component, in systolic time instant in relation to the average torsion

NAP200909C still spans a wider range than the other geometries, yet the median of 34% is still low compared to the maximum. The next two in order of decreasing difference are C0066 and C0075. The similarity between these three geometries is their higher torsion values. Looking at Fig. 8, the results show that below a threshold torsion, the velocity differences between the original and partial geometries in the systolic time instant are below 25%, while above this threshold are over 25%.

For the time-averaged results, the differences decrease, with all but one geometry having an IQR under 12% and a median below 10%. Looking at Fig. 9 the exception is again NAP200909C. It still has a higher IQR than the others with a median of 29%. The results for C0066_c have improved, the difference is lower than in the systolic and diastolic instances with a median of 3%.

The morphological parameters did not show any correlation for the agreement between the original and partial velocity fields. Torsion had the best results, as out of the five box plots shown, three had an increasing median with torsion. However, there were cases which did not always fit this trend, e.g. C0036 in Fig. 6.

The simulation time was on average 11.5 hours, while for the partial geometries it was 3 hours. This is a reduction of 74.8%. The cutting process only required less than 3 minutes of added time from humans as the workflow is highly automated.

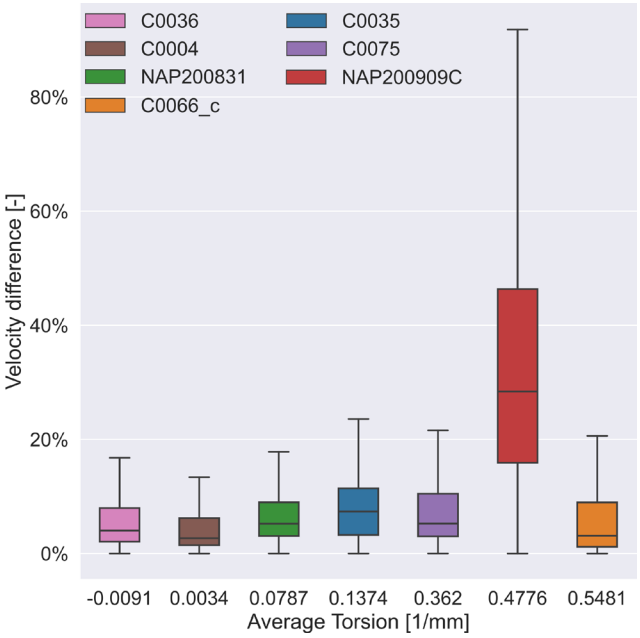

Fig. 9 Velocity difference graph for the secondary component, time averaged results in relation to the average torsion

4 Limitations

The scope of this article was severely limited. The seven examined cases are not sufficient to draw statistically significant conclusions from the results.

Blood was modelled as a Newtonian fluid and the walls of the vessels were assumed to be rigid.

5 Conclusions

The scope of this project was to evaluate a method to reduce the computational requirements of CFD simulations for bifurcation aneurysms after the ICA terminating bifurcation using a 0D method. The volumetric flow rates showed good agreement, in all cases the difference was below 1%. For the cycle-averaged axial velocity fields, the median difference between the original and the partial geometries stayed below 5% except for one case. These results are in line with the finding of [33].

The secondary velocity field had less promising results. In some cases, the differences were below 20% but in others, it was higher than 100%. Unfortunately, the differences did not show correlation to morphological parameters, although other parameters than the average torsion were also examined. The small cohort may also play a role. Therefore, this procedure cannot be used to reduce the computational domain if the secondary velocity field is of importance.

Funding

Péter Friedrich and his work were supported by the Gedeon Richter Talentum Foundation in the framework of the Gedeon Richter Excellence PhD Scholarship.

References

[1] Chalouhi, N., Hoh, B. L., Hasan, D. "Review of Cerebral Aneurysm Formation, Growth, and Rupture", Stroke, 44(12), pp. 3613–3622, 2013. https://doi.org/10.1161/STROKEAHA.113.002390

[2] Vlak, M. H. M., Algra, A., Brandenburg, R., Rinkel, G. J. E. "Prevalence of unruptured intracranial aneurysms, with emphasis on sex, age, comorbidity, country, and time period: a systematic review and meta-analysis", The Lancet Neurology, 10(7), pp. 626–636, 2011. https://doi.org/10.1016/S1474-4422(11)70109-0

[3] Wiebers, D. O., Torner, J. C., Meissner, I. "Impact of Unruptured Intracranial Aneurysms on Public Health in the United States", Stroke, 23(10), pp. 1416–1419, 1992. https://doi.org/10.1161/01.str.23.10.1416

[4] Sforza, D. M., Putman, C. M., Cebral, J. R. "Hemodynamics of Cerebral Aneurysms", Annual Review of Fluid Mechanics, 41, pp. 91–107, 2009. https://doi.org/10.1146/annurev.fluid.40.111406.102126

[5] Nakatani, H., Hashimoto, N., Kang, Y., Yamazoe, N., Kikuchi, H., Yamaguchi, S., Niimi, H. "Cerebral blood flow patterns at major vessel bifurcations and aneurysms in rats", Journal of Neurosurgery, 74(2), pp. 258–262, 1991. https://doi.org/10.3171/jns.1991.74.2.0258

[6] Sho, E., Sho, M., Singh, T. M., Xu, C., Zarins, C. K., Masuda, H. "Blood Flow Decrease Induces Apoptosis of Endothelial Cells in Previously Dilated Arteries Resulting From Chronic High Blood Flow", Arteriosclerosis, Thrombosis, and Vascular Biology, 21(7), pp. 1139–1145, 2001. https://doi.org/10.1161/hq0701.092118

[7] Boussel, L., Rayz, V., McCulloch, C., Martin, A., Acevedo-Bolton, G., Lawton, M., Higashida, R., Smith, W. S., Young, W. L., Saloner, D. "Aneurysm Growth Occurs at Region of Low Wall Shear Stress: Patient-Specific Correlation of Hemodynamics and Growth in a Longitudinal Study", Stroke, 39(11), pp. 2997–3002, 2008. https://doi.org/10.1161/STROKEAHA.108.521617

[8] Fukuda, S., Yasu, T., Predescu, D. N., Schmid-Schönbein, G. W. "Mechanisms for Regulation of Fluid Shear Stress Response in Circulating Leukocytes", Circulation Research, 86(1), pp. e13–e18, 2000. https://doi.org/10.1161/01.RES.86.1.e13

[9] Cebral, J. R., Castro, M. A., Burgess, J. E., Pergolizzi, R. S., Sheridan, M. J., Putman, C. M. "Characterization of Cerebral Aneurysms for Assessing Risk of Rupture By Using Patient-Specific Computational Hemodynamics Models", American Journal of Neuroradiology, 26(10), pp. 2550–2559, 2005.

[10] Emory University, Orobix Srl "AneuriskWeb: The Aneurisk dataset repository", 2012–2013. [online] Available at: http://ecm2.mathcs.emory.edu/aneuriskweb [Accessed: 05 September 2023]

[11] Ford, M. D., Hoi, Y., Piccinelli, M., Antiga, L., Steinman, D. A. "An objective approach to digital removal of saccular aneurysms: technique and applications", British Journal of Radiology, 82(special_issue_1), pp. S55–S61, 2009. https://doi.org/10.1259/bjr/67593727

[12] Bergersen, A. W., Chnafa, C., Gallo, D., Piccinelli, M., Steinman, D. A., Valen-Sendstad, K. "Automated and objective removal of bifurcation aneurysms: Incremental improvements, and validation against healthy controls", Journal of Biomechanics, 96, 109342, 2019. https://doi.org/10.1016/j.jbiomech.2019.109342

[13] Qian, Y., Takao, H., Umezu, M., Murayama, Y. "Risk Analysis of Unruptured Aneurysms Using Computational Fluid Dynamics Technology: Preliminary Results", American Journal of Neuroradiology, 32(10), pp. 1948–1955, 2011. https://doi.org/10.3174/ajnr.A2655

[14] Valen-Sendstad, K., Bergersen, A. W., Shimogonya, Y., Goubergrits, L., Bruening, J., Pallares, J., …, Steinman, D. A. "Real-World Variability in the Prediction of Intracranial Aneurysm Wall Shear Stress: The 2015 International Aneurysm CFD Challenge", Cardiovascular Engineering and Technology, 9(4), pp. 544–564, 2018. https://doi.org/10.1007/s13239-018-00374-2

[15] Berg, P., Voß, S., Saalfeld, S., Janiga, G., Bergersen, A. W., Valen-Sendstad, K., …, Beuing, O. "Multiple Aneurysms AnaTomy CHallenge 2018 (MATCH): Phase I: Segmentation", Cardiovascular Engineering and Technology, 9(4), pp. 565–581, 2018. https://doi.org/10.1007/s13239-018-00376-0

[16] Csippa, B., Závodszky, G., Paál, G., Szikora, I. "A new hypothesis on the role of vessel topology in cerebral aneurysm initiation", Computers in Biology and Medicine, 103, pp. 244–251, 2018. https://doi.org/10.1016/j.compbiomed.2018.10.018

[17] Cebral, J. R., Castro, M. A., Putman, C. M., Alperin, N. "Flow–area relationship in internal carotid and vertebral arteries", Physiological Measurement, 29(5), 585, 2008. https://doi.org/10.1088/0967-3334/29/5/005

[18] Chnafa, C., Brina, O., Pereira, V. M., Steinman, D. A. "Better Than Nothing: A Rational Approach for Minimizing the Impact of Outflow Strategy on Cerebrovascular Simulations", American Journal of Neuroradiology, 39(2), pp. 337–343, 2018. https://doi.org/10.3174/ajnr.A5484

[19] Chnafa, C. "aneuTools", [computer program] Available at: https://github.com/ChrisChnafa/aneuTools [Accessed: 02 April 2023]

[20] Friedrich, P., Csippa, B., Paál, G., Szikora, I. "Initiation of Bifurcation Aneurysms: A Piplot Study", In: Proceedings of the Conference on Modelling Fluid Flow (CMFF'22), Budapest, Hungary, 2022, pp. 379–384. ISBN 9789634218814

[21] BWH and 3D Slicer contributors "3D Slicer (5.0.3)", [computer program] Available at: https://www.slicer.org/ [Accessed: 13 November 2023]

[22] Taubin, G. "Curve and surface smoothing without shrinkage", In: Proceedings of IEEE International Conference on Computer Vision, Cambridge, MA, USA, 1995, pp. 852–857. ISBN 0-8186-7042-8 https://doi.org/10.1109/iccv.1995.466848

[23] Piccinelli, M., Veneziani, A., Steinman, D. A., Remuzzi, A., Antiga, L. "A Framework for Geometric Analysis of Vascular Structures: Application to Cerebral Aneurysms", IEEE Transactions on Medical Imaging, 28(8), pp. 1141–1155, 2009. https://doi.org/10.1109/TMI.2009.2021652

[24] Manini, S., Antiga, L. "Vascular Modelling Toolkit (1.4.0)", [computer program] Available at: http://www.vmtk.org/ [Accessed: 13 April 2023]

[25] Kitware, Inc. "ParaView (5.10.1)", [computer program] Available at: https://www.paraview.org/ [Accessed: 27 February 2023]

[26] Csippa, B., Sándor, L., Paál, G. "Decomposition of Velocity Field Along a Centerline Curve Using Frenet-Frames: Application to Arterial Blood Flow Simulations", Periodica Polytechnica Mechanical Engineering, 65(4), pp. 374–384. 2021. https://doi.org/10.3311/PPME.18517

[27] Ansys, Inc. "Ansys 22 R2", [computer program] Available at: https://www.ansys.com/ [Accesed: 23 January 2023]

[28] Morales, H. G., Larrabide, I., Geers, A. J., Aguilar, M. L., Frangi, A. F. "Newtonian and non-Newtonian blood flow in coiled cerebral aneurysms", Journal of Biomechanics, 46(13), pp. 2158–2164, 2013. https://doi.org/10.1016/j.jbiomech.2013.06.034

[29] Guerciotti, B., Vergara, C. "Computational Comparison Between Newtonian and Non-Newtonian Blood Rheologies in Stenotic Vessels", In: Wriggers, P., Lenarz, T. (eds.) Biomedical Technology: Modeling, Experiments and Simulation, Springer International Publishing, 2018, pp. 169–183. ISBN 978-3-319-59547-4 https://doi.org/10.1007/978-3-319-59548-1_10

[30] Kumar, N., Khader, A., Pai, R., Kyriacou, P., Khan, S., Koteshwara, P. "Computational fluid dynamic study on effect of Carreau-Yasuda and Newtonian blood viscosity models on hemodynamic parameters", Journal of Computational Methods in Sciences and Engineering, 19(2), pp. 465–477, 2019. https://doi.org/10.3233/JCM-181004

[31] Dempere-Marco, L., Oubel, E., Castro, M., Putman, C., Frangi, A., Cebral, J. "CFD Analysis Incorporating the Influence of Wall Motion: Application to Intracranial Aneurysms", In: 9th International Conference on Medical Image Computing and Computer-Assisted Intervention, MICCAI 2006, Copenhagen, Denmark, 2006, pp. 438–445. ISBN 978-3-540-44727-6 https://doi.org/10.1007/11866763_54

[32] Larrabide, I., Geers, A. J., Morales, H. G., Aguilar, M. L., Rüfenacht, D. A. "Effect of aneurysm and ICA morphology on hemodynamics before and after flow diverter treatment", Journal of NeuroInterventional Surgery, 7(4), pp. 272–280, 2015. https://doi.org/10.1136/neurintsurg-2014-011171

[33] Ugron, Á., Paál, G. "On the boundary conditions of cerebral aneurysm simulations", Periodica Polytechnica Mechanical Engineering, 58(1), pp. 37–45, 2014. https://doi.org/10.3311/PPme.7392